Elucidation of Structure–Activity Relations in Proton Electroreduction at Pd Surfaces: Theoretical and Experimental Study

Thorsten O. Schmidt, Apinya Ngoipala, Ryan L. Arevalo, Sebastian A. Watzele, Raju Lipin, Regina M. Kluge, Shujin Hou, Richard W. Haid, Anatoliy Senyshyn, Elena L. Gubanova,* Aliaksandr S. Bandarenka,* and Matthias Vandichel*

The structure–activity relationship is a cornerstone topic in catalysis, which lays the foundation for the design and functionalization of catalytic materials. Of particular interest is the catalysis of the hydrogen evolution reaction (HER) by palladium (Pd), which is envisioned to play a major role in realizing a hydrogen-based economy. Interestingly, experimentalists observed excess heat generation in such systems, which became known as the debated "cold fusion" phenomenon. Despite the considerable attention on this report, more fundamental knowledge, such as the impact of the formation of bulk Pd hydrides on the nature of active sites and the HER activity, remains largely unexplored. In this work, classical electrochemical experiments performed on model Pd(hkl) surfaces, "noise" electrochemical scanning tunneling microscopy (n-EC-STM), and density functional theory are combined to elucidate the nature of active sites for the HER. Results reveal an activity trend following Pd(111) > Pd(110) > Pd(100) and that the formation of subsurface hydride layers causes morphological changes and strain, which affect the HER activity and the nature of active sites. These findings provide significant insights into the role of subsurface hydride formation on the structure–activity relations toward the design of efficient Pd-based nanocatalysts for the HER.

1. Introduction

In the ongoing global process of decarbonization toward a sustainable future,[1,2] hydrogen has been extensively regarded as a sustainable, next-generation energy carrier due to its high energy density. Additionally, it is a carbon-free fuel, which can in principle be generated by water electrolysis all over the world.[3–5] To realize such a hydrogen-based economy,[6–8] it is imperative to gain a fundamental understanding of the interaction of hydrogen with (metal) catalysts. Evaluating these electrode materials' stability, activity, and selectivity is a key step to improving the hydrogen reaction kinetics. In particular, the structure–activity relation of interfacial electrode/electrolyte interactions are crucial for various technological applications that include hydrogen storage,[9,10] hydrogen sensing,[11,12] hydrogenation/dehydrogenation,[13,14] hydrogen purification/separation,[15,16] and electrocatalysis.[17–19]

Due to this expanding range of applications, especially hydrogen-metal systems have increasingly come to the forefront of the research community; more precisely, the interaction of hydrogen with metal catalysts such as platinum (Pt), palladium (Pd), or nickel has been extensively studied using a variety of experimental and computational techniques.[20–22] Among these metal catalysts, Pd has received a significant research interest for the study of metal-hydrogen interaction, as it can readily absorb large volumetric quantities of hydrogen at accessible temperatures and pressures, possesses a high hydrogen diffusion coefficient, and promotes a facile dissociation of hydrogen molecules at the surface.[23–26] Pd-based systems have previously been studied through both experimental techniques such as low-energy electron diffraction (LEED),[27–29] electron energy loss spectroscopy (EELS),[30,31] thermal desorption spectroscopy (TDS),[32] X-ray diffraction (XRD),[33] X-ray photoelectron spectroscopy (XPS);[34] and theoretical approaches such as semiempirical approaches like embedded-cluster methods[35] or effective-medium models[36] and ab initio methods based on density functional theory (DFT).[37,38] These reports, among

T. O. Schmidt, S. A. Watzele, R. M. Kluge, S. Hou, R. W. Haid,
E. L. Gubanova, A. S. Bandarenka
Physics of Energy Conversion and Storage
Department of Physics
Technical University of Munich
James-Franck-Straße 1, 85748 Garching, Germany
E-mail: elena.gubanova@tum.de; bandarenka@ph.tum.de
A. Ngoipala, R. L. Arevalo, R. Lipin, M. Vandichel
Department of Chemical Sciences and Bernal Institute
University of Limerick
Limerick V94 T9PX, Ireland
E-mail: matthias.vandichel@ul.ie
S. Hou, A. S. Bandarenka
Catalysis Research Center TUM
Ernst-Otto-Fischer-Str. 1, 85748 Garching, Germany
A. Senyshyn
Heinz Maier-Leibnitz-Zentrum (MLZ)
Technical University of Munich
Lichtenbergstr. 1, 85748 Garching, Germany

others, have identified the preferred adsorption/absorption -sites, -geometries, and -energies, surface diffusion, and electronic structures of H chemisorption on Pd(111), Pd(100), and Pd(110) surfaces. More interestingly, experimentalists observed an anomalous generation of excess heat in the Pd-catalyzed electrochemical hydrogen evolution reaction (HER), which later became known as the highly debated "cold fusion".[39–41] Despite the tremendous research interest that emerged from such reports, still, many questions concerning the structure–activity relation for hydrogen reactions on Pd surfaces remain unresolved. In particular, there is a lack of a comprehensive understanding of the dynamic behavior and surface mobility of Pd, the effect of subsurface hydride formation and lattice/surface strain on the HER activity, as well as the stability of the surface under HER conditions.

In this work, experimental and theoretical tools were used to assess the complexity and dynamics of such Pd-hydrogen systems, focusing on the low-indexed basal planes Pd(111), Pd(110), and Pd(100) as well as on the stepped Pd(211) surface. For this purpose, findings of XRD, electrochemical impedance spectroscopy (EIS), "classical" electrochemical activity and electrochemical scanning tunneling microscopy (EC-STM) measurements as well as DFT-based calculations were combined, leading to a bigger picture of hydrogen-induced changes in the lattice strain, diffusion behavior, electrochemical activity, and the morphology of the Pd surface. Correspondingly, we present the 3-state free energy diagrams for HER activities on the Pd basal planes with different numbers of Pd hydride sublayers as well as the effect of the surface coverage on the areal strain. The resulting transformation of the surface morphology and the consequent influence on the active sites are experimentally shown in detail for Pd(111) and Pd(100) by using "noise" EC-STM (n-EC-STM).[42,43] For this purpose, the nature of active sites of both Pd single crystals is elucidated before and after hydrogen absorption. To the best of our knowledge, this work reports for the first time the HER activity trends for different Pd(hkl) model systems obtained from systematic measurements and calculations that take into account the effect of subsurface hydride formation in structure–activity relations. These findings contribute to a better understanding of the complex and dynamic processes at the Pd surface and sublayers in correlation with hydrogen ad- and absorption.

2. Results and Discussion

In the following, several theoretical and experimental tools are applied to investigate the nature of hydrogen ad- and absorption on the single crystalline Pd planes (111), (110), (100), and (211).

2.1. Hydrogen Absorption Behavior, Surface Mobility of Pd, Reaction Mechanism, and Kinetics

To compare the relative stabilities of the Pd(111), Pd(100), Pd(110), and Pd(211) surfaces, their surface energies were calculated. The computational details are provided in Section S1 (Supporting Information). The obtained surface energies are

0.132, 0.150, 0.145, and 0.147 eV Å^{-2} for pristine Pd(111), Pd(110), Pd(100), and Pd(211) surfaces, respectively, and indicate that the Pd(111) surface is the most stable, followed by the Pd(100) surface. Furthermore, the stepped Pd(211) surface is more stable than the Pd(110) surface. This is reasonable as the Pd(211) surface is composed of Pd(111) terrace sites and a step that has a Pd(100) character, while the Pd(110) surface has a more open structure. Note that the order of these three low-index surface energies, [Pd(111) < Pd(100) < Pd(110)], is in good agreement with the results from previous theoretical studies on the surface energies of the fcc-metals.[44,45] Our finding indicates that the Pd(111) surface is expected to be the most dominant surface in a Pd nanostructure.

Next, the electrochemical behavior of the annealed Pd(hkl) model surfaces was investigated using a cyclic voltammetry method. Cyclic voltammograms (CV) were recorded and compared for the Pd(111), Pd(110), and Pd(100) surfaces in a potential range between 0.2 and 1.2 V versus a reversible hydrogen electrode (V_{RHE}) in Ar-saturated 0.1 M HClO$_4$. A continuous change of the CV shapes was observed over time until the system stabilized after more than 30 cycles (Figure S2, Supporting Information). Previous literature[23–26,46] suggests that hydrogen adsorption and absorption play a pivotal role. The interplay of these processes is assumed to explain the dynamic behavior (morphological changes) of the Pd surfaces, which occurred under electrochemical reaction conditions. Therefore, only the first cycles of the typical CVs (**Figure 1**a–c) are considered to be representative for the freshly annealed surfaces of Pd single crystals. Since the recorded CVs are in good agreement with the literature data,[47,48] the successful preparation of well-defined single crystalline surfaces was confirmed. It should be noted that further measurements were performed with the as-prepared (freshly annealed) surface, while the number of cycles was reduced to the minimum to avoid surface reconstruction.

For further evaluation of the adsorption and subsequent absorption process, the hydrogen under-potential deposition (H$_{UPD}$) region was closely examined. For this, the anodic and cathodic peaks were integrated and compared as shown in Figure 1a–c. On the freshly annealed Pd(111), the cathodic scan yielded an integrated charge (Q_c) of ≈290 µC cm^{-2} (Figure 1a). For comparison, one monolayer (ML) of adsorbed hydrogen on Pt(111) corresponds to a charge of ≈240 µC cm^{-2}.[49,50] Due to the observed charge, higher than the theoretically expected value for 1 ML of hydrogen, indicates that a possible absorption of adsorbed protons might have occurred. In contrast, the integrated anodic scan (Q_a) on Pd(111) returned only a charge of ≈225 µC cm^{-2}. This implies that only ≈78% ($Q_a/Q_c = 0.78$) of the protons got oxidized during the anodic scan, and therefore ≈22% was absorbed into the bulk. The highest hydrogen absorption was detected for Pd(110), as visible in Figure 1b. Here, only ≈69% of the produced hydrogen got oxidized during the anodic scan, meaning that ≈31% was absorbed into the bulk. The total value of the integrated cathodic scan of this crystal was ≈145 µC cm^{-2}, so half of the one for Pd(111). A possible explanation for this could be a lower number of available active sites. For the freshly annealed Pd(100) only ≈12% of the produced hydrogen was absorbed into the bulk in the first cycle (Figure 1c). This results in an adsorption/desorption ratio of $Q_a/Q_c = 0.88$. In summary, this electrochemical behavior of the
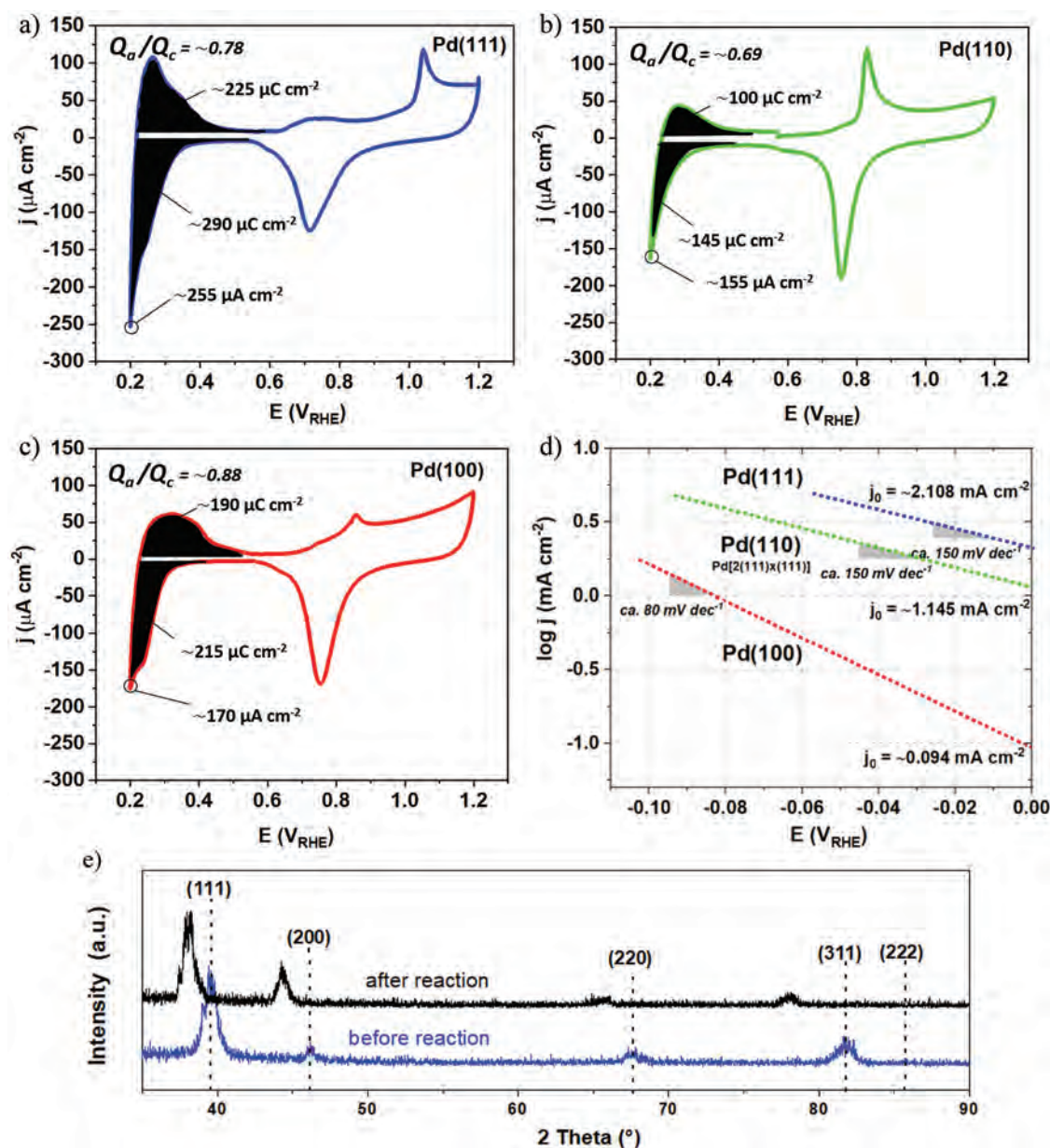
Figure 1. The first scans of the CVs of the annealed a) Pd(111), b) Pd(110), and c) Pd(100) single crystals in Ar-saturated 0.1 M HClO₄ recorded at a scan rate of 50 mV s⁻¹. d) Tafel plots of the HER activity on the Pd(111), (110), and (100) single crystals, recorded in H₂-saturated 0.1 M HClO₄ with a scan rate of 50 mV s⁻¹. e) Grazing-incidence XRD patterns of single-crystalline Pd(111) before and after HER (6 cycles) indicate peak shifts from the pristine Pd electrode to PdH$_{0.72}$.

Pd surface can indicate that even after a single electrochemical cycle, a certain amount of hydrogen absorbs into the Pd bulk.

The Tafel plots in Figure 1d present the activity trend of the Pd(111), (110), and (100) surfaces for the HER, using an experimentally estimated exchange current density (j_0), as discussed below. Tafel plots as well as Tafel slopes are typically used to identify the rate-determining step of the HER. In particular, Tafel slope values of 30, 40, and 120 mV dec⁻¹ are typically associated with Tafel, Heyrovsky, and Volmer as possible rate-determining steps (RDS), respectively.[51] However, in reality, the Tafel slopes frequently change over the potential and do not always adopt one of the theoretical values, which

makes it difficult to determine the RDS. Remarkably, for both Pd(111) and Pd(110) the estimated Tafel slope values were equal to 150 mV dec⁻¹, while for Pd(100), it was found to be ≈80 mV dec⁻¹. This finding indicates that the energetic and geometrical properties of the most active sites on Pd(111) and Pd(110) could be similar, while they are different from these of Pd(100). The exchange current densities of the Pd electrodes were calculated by extrapolating the Tafel plots. The values of ≈2.108, ≈1.145, and ≈0.094 mA cm⁻² for Pd(111), Pd(110), and Pd(100), respectively, were estimated. Additionally, we calculated the exchange current densities by DFT and rendered a volcano plot, as shown in Figure S3 (Supporting Information). The

experimentally observed trend was confirmed by these theoretically obtained results, which will be presented in the following.

The influence of the absorbed hydrogen on the lattice parameter was investigated by XRD measurements for the most active Pd single crystal, i.e., Pd(111). For this purpose, XRD patterns were recorded for the pristine sample and for the sample after six cycles of HER (Figure 1e). The results indicated a lattice parameter of 3.89 Å before the HER and about 4.07 Å after the HER, corresponding to an H:Pd ratio of about 0.72 (extrapolated on the basis of data from ref. [52]). This corresponds to a relative lattice expansion of ≈4.6%, suggesting an increased surface strain. Investigations of the surface strain and its effects on the morphology and local electrochemical activity are discussed in Section 2.3.

Further, EIS was applied to investigate the reaction mechanism and kinetics at the Pd single crystal surfaces. For this purpose, spectra were recorded at $-30\,mV_{RHE}$ allowing to probe the electrified interface during the HER, without significant noise that could be caused by stochastic surface blockage by $H_2(g)$ at higher overpotentials. **Figure 2**a–c shows the EIS spectra of Pd(111), Pd(110), and Pd(100), respectively. The Nyquist plots of the three investigated surfaces have a similar shape, consisting of an almost perfect semicircle in the high-frequency regime and a transition to an ≈ 45° regime at lower frequencies. The latter indicates some diffusion limitations of the reaction kinetics.

In a previous work,[53] we showed a model to analyze the dominating reaction mechanism on Pt surfaces. With this, a distinction can be made between the Volmer–Heyrovsky mechanism and the Volmer–Tafel mechanism. Briefly, the Faradaic part of the equivalent electrical circuit (EEC) consists of one branch reflecting the reaction kinetics of the Volmer–Heyrovsky and another reflecting the kinetics of the Volmer–Tafel mechanism. The former consists of a charge transfer resistance, in series with an adsorption capacitance and adsorption resistance in parallel, while the Volmer–Tafel branch consists of only a charge transfer resistance and a Warburg diffusion element.[53] Applying the same EEC to the impedance spectra of the Pd surfaces shown in Figure 2a–c, it was possible to fit them appropriately. However, the charge transfer resistance of the Volmer–Heyrovsky branch is extremely high, and the adsorption capacity is rather undefined values. The relatively high charge transfer resistance indicates that the reaction kinetics of this branch is comparatively slow. Further, the large uncertainties of the adsorption capacitance imply that this parameter contributes only little to the overall fitting. This, and the fact that an excellent fit of the impedance is achieved with only the Volmer–Tafel branch, show that the Volmer–Heyrovsky mechanism plays a subordinate role at most. Therefore, the equivalent circuit shown in Figure 2d was used for further analysis. Applying this EEC, the root-mean-square deviation of the fitting is less than 1%. Further, individual parameters show low uncertainties, which asserts the accuracy of the model for describing the impedance response of the electrochemical system. The applicability of this EEC indicates the Volmer–Tafel and or the direct absorption of protons as the dominating mechanism for the Pd surfaces at low overpotentials. Note that the EEC for both processes is indistinguishable. In any case, most of the generated hydrogen was directly absorbed as no formation of hydrogen bubbles was detected.

To further analyze the electrified interface, we focus on the parameters of the Faradaic branch: the charge transfer
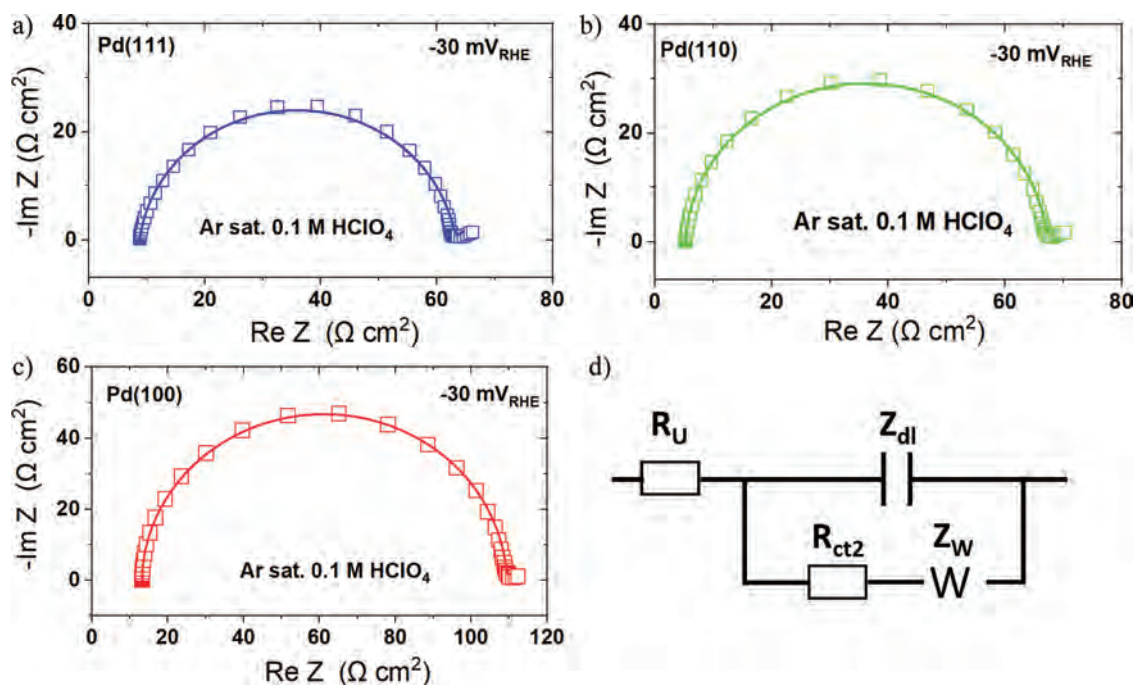

Figure 2. Impedance data of different Pd single crystal surfaces recorded in Ar-saturated 0.1 M $HClO_4$ electrolyte, represented as Nyquist plots. a–c) shows spectra of the Pd(111), Pd(110), and Pd(100), respectively. Open symbols represent measured data points, and the line corresponds to fitting using the EEC shown in (d). The EEC consists of a constant phase element to fit the response of the electrochemical double layer and a charge transfer resistance in series with a Warburg element, accounting for reaction kinetics and mass transfer.

ADVANCED
SCIENCE NEWS
www.advancedsciencenews.com

NANO · MICRO
small
www.small-journal.com

resistance R_{ct} and the Warburg coefficient A_W.[54] The ratio of both parameters was determined as $\frac{A_W}{R_{ct}} \approx 0.02412$ s$^{-0.5}$, ≈ 0.02695 s$^{-0.5}$, ≈ 0.02392 s$^{-0.5}$ for Pd(111), Pd(110), and Pd(100), respectively. As shown in Section S4 in the Supporting Information, this allowed to roughly estimate the H coverage of Pd(111), Pd(110), and Pd(100) as ≈ 0, 0.3–0.4, and ≈ 0.95, respectively. This indicated that Pd(111) and Pd(110) have a rather low surface coverage while the surface of Pd(100) was almost entirely covered.

2.2. In Situ Active Site Investigation of as-Prepared Pd Surfaces

After verifying a well-defined surface structure, n-EC-STM was employed to elucidate the nature of active sites of the freshly annealed Pd. Note that "freshly annealed" means annealed according to Section 4, without any previous CV measurements before the experiment. Standard STM measurements of these freshly annealed single crystals are illustrated in Figure S4 of the Supporting Information. On both crystals, completely flat areas and sections with a roughness of approximately the height of one Pd atom were found (cf. Figure S4, Supporting Information). These measurements further confirm the surface quality. More details on the working principle and applications of the n-EC-STM technique can be found in Section 4 as well as in previous literature.[42,43,55–59] In short, the level of noise in the STM signal under reaction conditions serves to identify the active sites experimentally. As the reaction causes perturbations of the tunneling barrier, noise spikes will superimpose active areas in the images. In contrast, nonactive areas will be rather noise-free. Since the catalytically best and the worst performing crystals were Pd(111) and Pd(100) (Figure 1d), respectively, we employed the method to these surfaces, starting with the freshly prepared samples.

To choose adequate potentials for HER "On" and "Off," potential sweeps were carried out in the STM set-up against a Pt quasi–reference electrode (RE) (Figure S5, Supporting Information). For HER "On," the potential was chosen between −0.7 and −0.8 V versus Pt (V_{Pt}) in order to maintain a low reaction rate and thus minimize possible morphological changes. For HER "Off" the potential was set to 0.0 V_{Pt}, as here the current is practically zero. **Figure 3**a shows a typical noise measurement on Pd(111) in 0.1 M HClO$_4$. Four steps of different heights are visible, separating two atomically flat terraces (compare Figure S6, Supporting Information). Multiple line scans (height profile in fast scan direction) were extracted near the border of the potential change from "On" (black) to "Off" (red) and were stacked on top of each other for comparison. The different noise levels imply that the highest activity on the Pd(111) surface can be found on step edges, while the terraces are less active. As expected, for reaction "Off," the STM signal is noise-free, ensuring that the evaluated noise indeed stems from reaction processes instead of, e.g., shot noise or thermal noise. In addition, it is important to note that the captured step edges exhibited different noise levels, as demonstrated by the histograms in Figure 3b. More information on the noise analysis can be found in Section 4; and in Section S7 of the Supporting Information.

A similarly high step separating two terraces is visible in Figure 3c on freshly annealed Pd(100). An additional image showing a larger scale of this image can be found in Figure S7 (Supporting Information). Near the upper part of the step edge, some distinct noise spikes appeared for HER "On," and all the noise disappears for HER "Off." The right lower graph shows the difference between an active site at the step (black) and an adjacent nonactive site (red), both for reaction "On." The noise features were only observed at a few positions along the edge, which indicates a low density of active sites and, therefore, a low impact of the steps on the overall surface activity. Additionally, the noise was detected homogeneously across the terraces, which indicates activity all over the sample. The behavior of the terraces was further analyzed in the histograms in Figure 3d, showing a broader curve for the HER "On" data compared to HER "Off." It is important to note that a direct comparison of the terraces on Pd(111) and Pd(100) in Figure 3d is not possible due to specific individual experimental conditions, e.g., the shape and noise sensitivity of the STM-tip vary between individual measurements. However, a clear trend in the noise behavior of each measurement is observable. Unfortunately, STM is not able to detect the orientation of the step sites under these conditions. Note that only the low-index planes of Pd were investigated experimentally. The inclusion of Pd(211) in the theoretical considerations merely served as a model system for the step sites on the Pd surfaces that were observed especially in the n-EC-STM measurements. Nevertheless, we can assume that the differences in local activity for different step sites may originate from differences in local coordination or orientation.

2.3. The Strain Effect on the HER Activity

Since we observed hydrogen absorption during the experiments, together with an alteration of the surface lattice parameter from XRD measurements, the Pd hydride formation was further investigated using DFT calculations. It has been found from neutron diffraction studies that the hydrogen atoms in Pd hydride randomly occupy the octahedral interstices in the Pd-metal lattice.[60,61] This result is also supported by DFT studies.[62] For this reason, the formation of a Pd hydride (PdH$_x$) was investigated by initially populating the octahedral sites of an fcc bulk Pd crystal, followed by the tetrahedral sites. That is, the hydrogen atoms occupy the octahedral interstices only for $x \leq 1$. The calculated formation energies shown in Figure S8 (Supporting Information) indicate that the most stable Pd:H ratio is 1:1, in agreement with other DFT studies.[62,63] Interestingly, all PdH$_x$ crystals with $x < 1.50$ are energetically feasible (i.e., formation energy is negative). This suggests that the hydrogen atoms in a PdH$_x$ can stably occupy both the octahedral and tetrahedral interstices. After all the octahedral interstices are occupied ($x = 1$), the additional hydrogen atoms can stably reside in the tetrahedral interstices for up to a Pd:H ratio lower than 1.50. Moreover, the calculated lattice constant of 3.891 Å for pure Pd is in good agreement with the experimental result, where the lattice constant of the pristine Pd(111) surface determined by XRD (Figure 1e) was 3.890 Å. Under electrochemical conditions, the DFT-calculated Pourbaix diagram for bulk PdH$_x$ (Figure S9, Supporting Information)
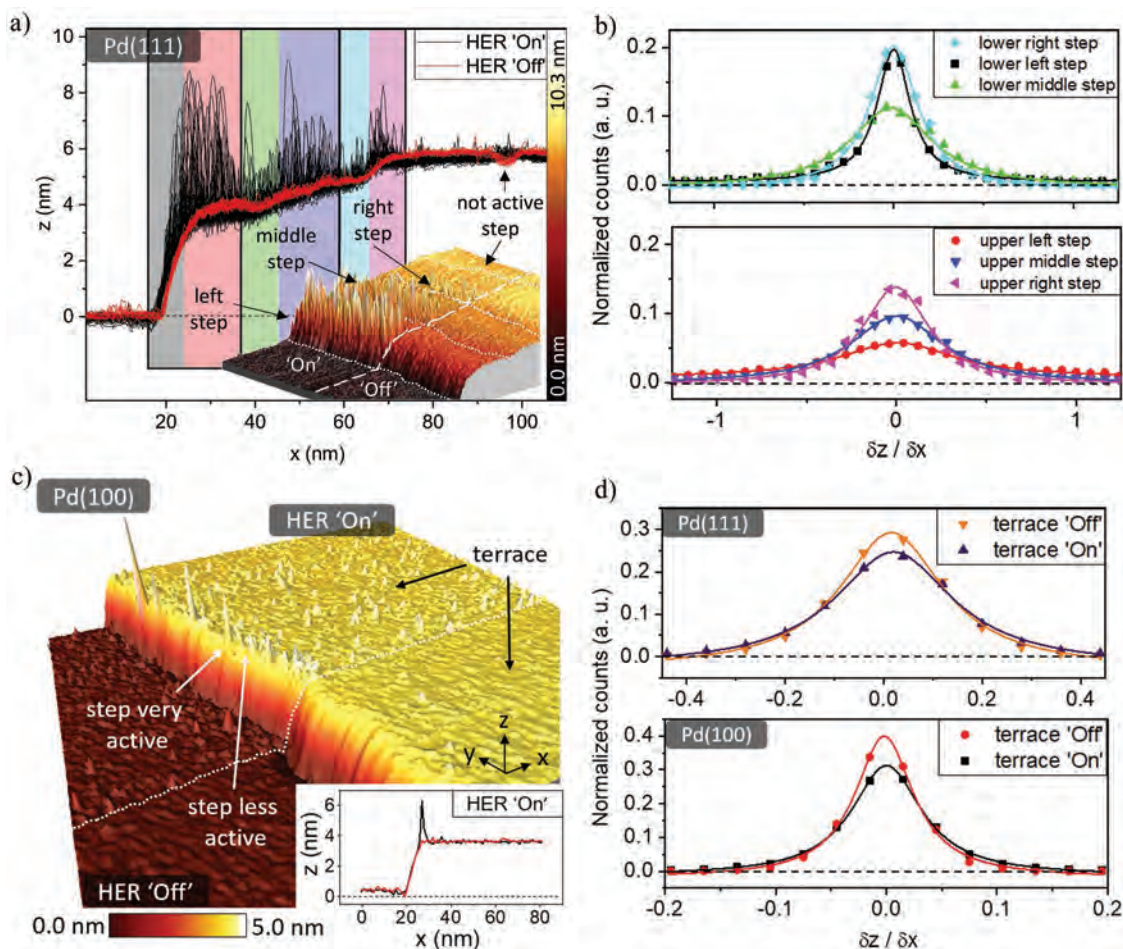
**ADVANCED
SCIENCE NEWS**

www.advancedsciencenews.com

**NANO · MICRO
small**

www.small-journal.com

Figure 3. n-EC-STM measurements of freshly annealed Pd(111) and Pd(100) in 0.1 M HClO₄ for the HER turned "On" at –0.7 V_{Pt} and "Off" at 0.0 V_{Pt}. a) 3D n-EC-STM image of Pd(111) and corresponding line scans, which were extracted close to the potential change from HER "On" (black) to HER "Off" (red). According to noise spikes, we observed active step sites and inactive terraces. b) Histograms of the signal derivatives at the vicinity of the three step edges, color code according to the background of the line scans in (a). A high noise level yields a broad and low-intensity histogram (see details in text). c) Multiatomic step on an otherwise atomically smooth Pd(100) surface. Here, under HER "On" conditions, the terraces exhibited electrocatalytic activity. The highest activity was found scattered along the upper step edge. In the inset, the adjacent line scans for HER "On" illustrate the difference in the noise level if high noise (black) or no noise (red) appears at the step. d) Histograms of the lower terrace of Pd(111) in (a) and the upper terrace of Pd(100) in (c), showing increased activity for HER "On."

shows that in the region around the equilibrium potential and pH for the HER, the most stable Pd:H ratio is 1:1. This agrees with the earlier noted result that such a Pd:H ratio is the most thermodynamically stable (Figure S8, Supporting Information). For a particular pH, shifting the electrode potential into more negative values increases the amount of hydrogen in bulk. The details for the calculation of the Pourbaix diagram are provided in Section S9 (Supporting Information).

Additionally, it is interesting to evaluate the effect of the formation of PdH sublayers on the stability of the Pd model surfaces. To this end, the surface energies of Pd(111), Pd(110), Pd(100), and Pd(211) surfaces containing different numbers of PdH sublayers were examined. First, we investigated the most stable absorption configuration of the H in the subsurface, where the Pd(111) surface was taken as a representative system as it is the close-packed structure, which is the most stable among the other more open surfaces. In this regard, the absorption energies of three possible H absorption sites, namely,

octahedral site, upper tetrahedral site, and lower tetrahedral site were calculated for the Pd(111) surface, as shown in Figure S10 (Supporting Information). Here, it can be seen that H is most strongly absorbed in the octahedral site, followed by lower and upper tetrahedral sites. Therefore, all surfaces containing zero to four PdH sublayers with H atoms at the octahedral sites were considered to calculate the surface energies. As demonstrated in Figure S1 (Supporting Information), the surface energies for Pd(111), Pd(110), Pd(100), and Pd(211) surfaces decrease as the number of PdH subsurface layer increases. This result indicates that the surfaces containing hydrogen subsurfaces are more stable than the corresponding clean surfaces. Therefore, it is crucial to examine the HER activity of the surfaces with different numbers of PdH sublayers in the model systems. To this end, we investigated the hydrogen atom adsorption (H*; where "*" denotes a surface-bound species) on the Pd(111), Pd(110), Pd(100), and Pd(211) surfaces containing different numbers of PdH subsurface layers in the near-surface region, with a

1:1 Pd:H ratio and with H atoms at the octahedral sites. The most stable H adsorption configuration for all four Pd surfaces was explored by comparing the adsorption energies of H* at the high symmetry sites of these surfaces (see Figure S11, Supporting Information). As reported in Tables S1–S4 (Supporting Information), H* is most stable at the fcc hollow site, pseudo-threefold site, fourfold hollow site, and fcc hollow site for the Pd(111), Pd(110), Pd(100), and Pd(211) surfaces, respectively. All of these identified stable adsorption sites for H* agree with previous theoretical studies.[64,65] Accordingly, the adsorption energies of H* on different Pd surfaces with different numbers of PdH sublayers were calculated in the most favorable adsorption sites. Before investigating the HER activity on all surfaces with hydrogen subsurfaces, we remark on the diffusion mechanism of the adsorbed H atom on the surface and in the subsurfaces (up to the fourth subsurface layer) to understand the behavior of the H atom after adsorbing on the surface. Here, the Pd(111) surface was taken as a representative system for H diffusion, where the diffusion path of the H atom passes through the fcc hollow site on the surface, then through the first, second, third, and fourth octahedral (O) sites in the subsurfaces (see Figure S12a, Supporting Information). We carried out climbing image nudged elastic band (CI-NEB) calculations to determine the minimum energy path and the corresponding diffusion barrier. The energy profile of the considered diffusion path of the H atom is illustrated in Figure S12b (Supporting Information). According to this diagram, the H atom has to overcome a barrier of 0.53 eV to move from the fcc hollow site on the surface to the first subsurface O site. This result is consistent with the previous theoretical study where the diffusion barrier obtained by the DFT potential energy surface was found to be 0.57 eV.[66] For the subsequent steps, the H atom diffuses from the first subsurface O site (1st sub O) to 2nd sub O, from 2nd sub O to 3rd sub O, and from 3rd sub O to 4th sub O, with barriers of 0.38, 0.31, and 0.21 eV, respectively. The H diffusion barrier of 0.21 eV from 3rd sub O to 4th sub O, i.e., passing through the bulk region is in good agreement with the experimental value of 0.23 eV for the H diffusion barrier in the Pd bulk.[67]

We now turn to evaluate the HER activity on the Pd(111), Pd(110), Pd(100), and Pd(211) surfaces with zero to four PdH sublayers. In terms of hydrogen electrocatalysis, the Gibbs free energy change of hydrogen atom adsorption, ΔG_{H*} is a widely accepted descriptor for the HER activities of various catalysts,[68] where a value of ΔG_{H*} that is close to zero (thermoneutral) indicates a good catalyst for the HER. To obtain ΔG_{H*}, we considered the hydrogen adsorption step (Volmer reduction) on surfaces with and without PdH subsurface layers, evaluated at $U_{SHE} = 0$, T = 300 K and P = 1 atm. The details for the calculation of ΔG_{H*} are provided in Section S9 (Supporting Information). Here, a low H* coverage was used to reflect the HER activity that corresponds to our experimental observation discussed earlier (Section 2.1). The H* coverage is defined as the number of the adsorbed H atoms divided by the number of exposed atoms of the corresponding clean surface in units of ML (monolayer). Therefore, the ΔG_{H*} at a low H* coverage of 1/4, 1/8, 1/4, and 1/6 ML for Pd(111), Pd(110), Pd(100), and Pd(211), respectively, was calculated and the 3-state free energy diagrams for the HER on the four surfaces with different numbers of PdH sublayers are illustrated in **Figure 4**.

For reference, the free energy diagrams for the high H* coverage cases (1 ML for all surfaces studied) are presented in Figure S13 (Supporting Information). We first discuss the HER activity on clean surfaces without PdH sublayer (0 PdH_{sub}). The ΔG_{H*} on pristine Pd(111), Pd(110), Pd(100), and Pd(211) surfaces are −0.427, −0.367, −0.474, and −0.386 eV. When H atoms are absorbed in the subsurface layers, the absolute values of ΔG_{H*} on the corresponding Pd(111), Pd(110), Pd(100), and Pd(211) surfaces tend to decrease, indicating an improvement for the HER performance. The values of ΔG_{H*} on the Pd(211) and Pd(111) surfaces that contain three to four PdH subsurface layers are much closer to zero; thus, these surfaces would display better HER activities, compared with those of all clean surfaces. The lower HER activities on all pristine surfaces arise from the strong adsorption energy of H* on the surface of Pd, which leads to weaker hydrogen desorption and active site poisoning. Note that all considered Pd(100) surfaces show large magnitudes of ΔG_{H*}, which would explain the inferior HER performance observed in the electrochemical measurements. For all surfaces with the highest number of PdH sublayers (4PdH_{sub}), the trend of increasing HER activity, i.e., the decreasing magnitude of ΔG_{H*} [Pd(100); −0.419 eV → Pd(110); −0.244 eV → Pd(111); −0.154 eV → Pd(211); −0.134 eV], is in excellent agreement with our experimental results that found the Pd(111) surface to exhibit the best HER performance, followed by the Pd(110) and Pd(100) surfaces (see Figure 1d).

It is interesting to note that the existence of different numbers of PdH subsurface layers significantly changes the HER activity for all surfaces. To obtain insights into the effect of an increasing number of PdH sublayers on the enhanced electrochemical HER activity, the geometric properties, i.e., lattice parameters of all considered surfaces, were investigated upon the formation of PdH subsurfaces. Since the volume of the bulk PdH increases as the Pd:H ratio increases (Figure S8, Supporting Information), the PdH subsurface layers that are formed on top of pure Pd are compressed, resulting in compressive strain. In **Figure 5**, the ΔG_{H*} and compressive areal strain for all studied surfaces at low H* coverage were plotted as a function of the number of PdH subsurface layers. The results for the high H* coverage cases are also provided in Figure S14 (Supporting Information). As noted earlier, a surface that has the value of ΔG_{H*} that is close to zero can be regarded to exhibit excellent HER activity. From Figure 5a, it can be assumed that when the first PdH subsurface is formed in the Pd(111) surface, ΔG_{H*} changes from −0.427 eV (bare surface) to −0.287 eV. This means that the presence of subsurface hydrogen significantly decreases the magnitude of the H* binding energy, which results in a higher HER activity compared to without PdH subsurface. This finding is consistent with a previous theoretical study that found the Pd subsurface H to destabilize the adsorbed H, which led to an increased reaction rate for ethyl hydrogenation.[69] A compressive areal strain of 1.44% occurs when the first and second subsurface layers are completely occupied by absorbed H atoms. As a result, the corresponding surface is more active for HER with a ΔG_{H*} of −0.209 eV. Upon the formation of three PdH sublayers, ΔG_{H*} is found to be −0.171 eV, where the surface is subjected to 3.16% areal compression. Finally, when the fourth PdH subsurface is reached, the Pd(111) surface is
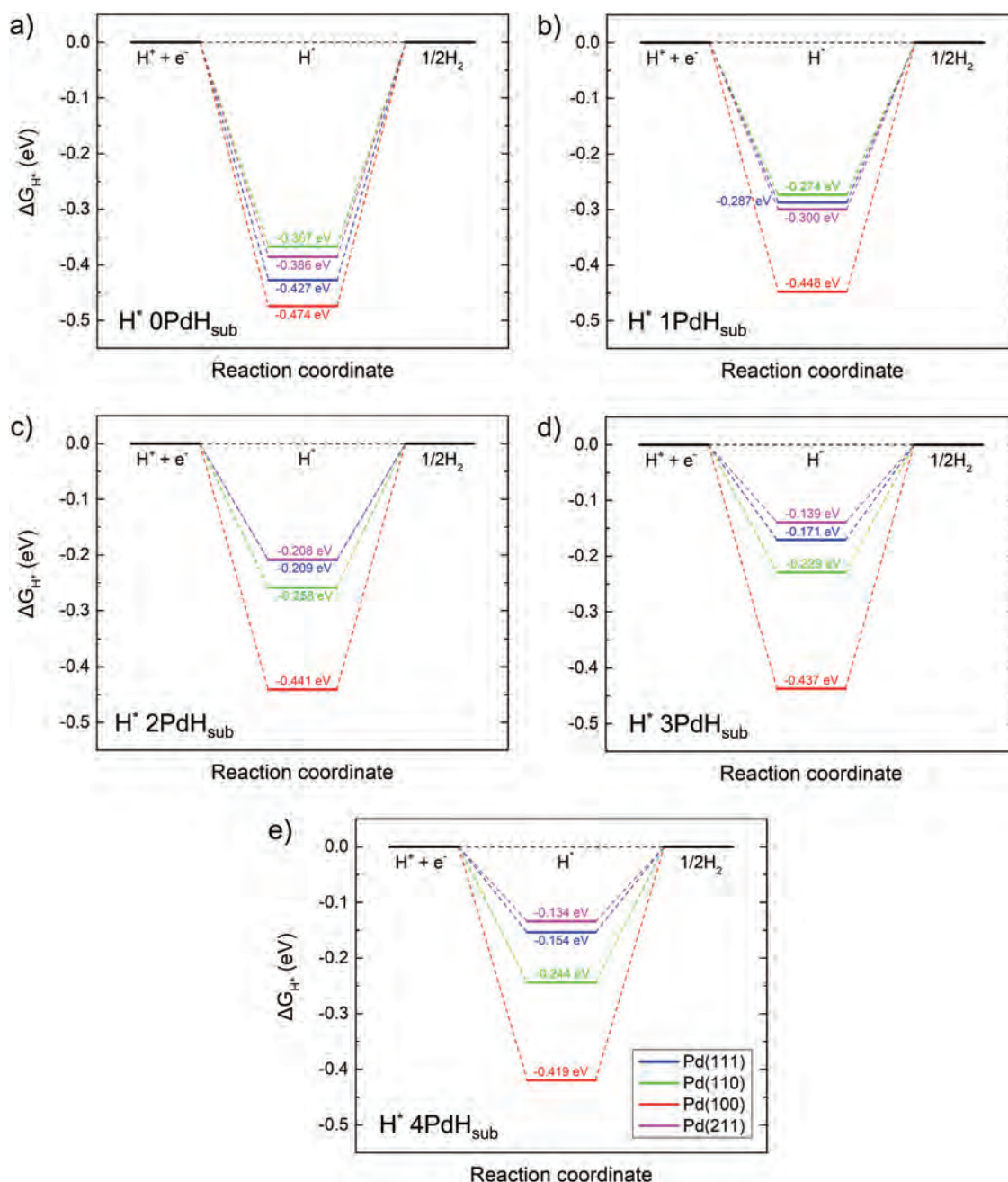
Figure 4. Free energy diagram for HER at low H* coverage on the Pd(111), Pd(110), Pd(100), and Pd(211) surfaces with zero to four PdH sublayers.

compressed with 4.18% areal strain, and the ΔG_{H*} gets closer to zero (−0.154 eV). These results indicate that the increase in compressive strain by the formation of PdH subsurfaces leads to weaker adsorption energy of H* on the surface and thus a higher HER activity. For the Pd(110) surface, the compressive areal strain is 0.77% upon hydrogen absorption in the first sublayer (Figure 5b). Such strain causes the change in the value of ΔG_{H*} from −0.367 eV on the bare surface to −0.274 eV. The Pd(110) surfaces with two and three PdH sublayers have compressive areal strains of 1.08% and 2.00%, and ΔG_{H*} values of −0.258 and −0.229 eV, respectively. Remarkably, in the presence of four PdH sublayers on the Pd(110) surface, the absolute

value of ΔG_{H*} slightly increases (−0.244 eV) although a large compressive areal strain (2.87%) is observed. For the Pd(100) surface (Figure 5c), the ΔG_{H*} values are −0.448 and −0.441 eV for the surface with one and two PdH sublayers, respectively (c.f., ΔG_{H*} = −0.474 eV for the pristine surface). Note that there is no strain observed until three subsurface H layers are reached. The surface with three PdH sublayers has a compressive areal strain of 0.70% and shows a ΔG_{H*} of −0.437 eV. When four PdH sublayers are formed, a compressive areal strain of 1.85%, and a ΔG_{H*} of −0.419 eV are found. These results indicate that the ΔG_{H*} on Pd(100) surfaces are relatively insensitive to the number of PdH sublayers and strain. For the Pd(211)
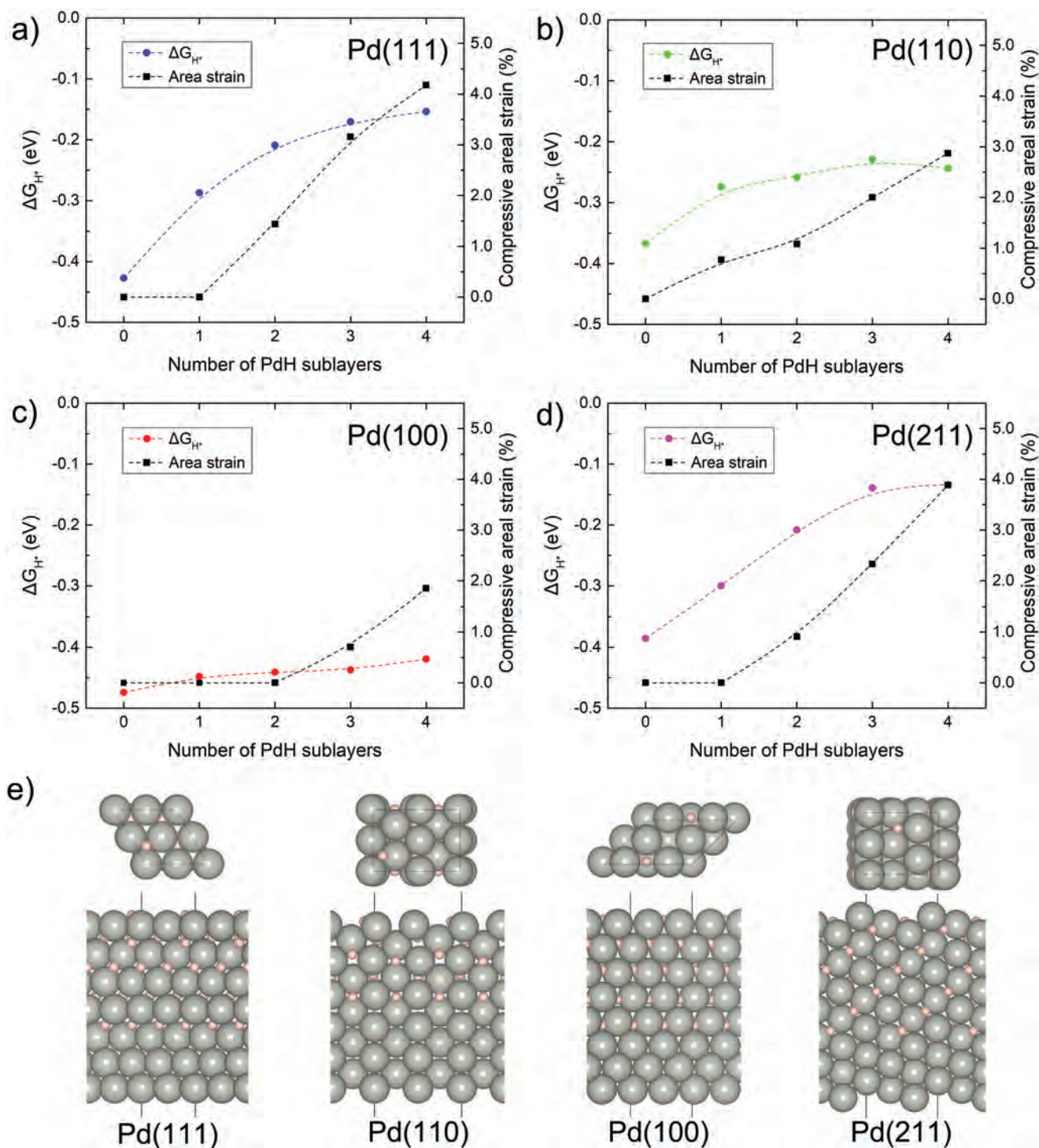
**ADVANCED
SCIENCE NEWS**

www.advancedsciencenews.com

NANO · MICRO
small

www.small-journal.com

Figure 5. Hydrogen adsorption free-energy change (ΔG_{H*}) at low H* coverage and compressive areal strain as a function of the number of PdH sublayers for a) Pd(111), b) Pd(110), c) Pd(100), and d) Pd(211) surfaces. The compressive areal strain, ε_A, is defined as $\varepsilon_A(\%) = \frac{A_{uc} - A_c}{A_c} \times 100$, where A_{uc} and A_c are the areas of the unconstrained and constrained PdH/Pd interface systems, respectively. e) The structural configurations of H* on the surface with four PdH sublayers (i.e., largest strain considered) for all studied surfaces.

surface, as the PdH sublayers and strain increase, the trend of the decrease in the magnitude of ΔG_{H*} is very similar to that of the Pd(111) surface. As displayed in Figure 5d, while there is no strain occurring when the first PdH sublayer is formed, ΔG_{H*} changes from −0.386 eV (bare surface) to −0.300 eV. For the surface with two, three, and four PdH sublayers which possess a compressive areal strain of 0.91%, 2.33%, and 3.89%, respectively, their ΔG_{H*} values approach zero (−0.208, −0.139, and

−0.134 eV, respectively). Comparing all surfaces with four PdH sublayers (i.e., largest strain considered), a trend of increasing compressive areal strain was observed [Pd(100); 1.85% → Pd(110); 2.87% → Pd(211); 3.89% → Pd(111); 4.18%], whereas a decreasing trend of the magnitude of ΔG_{H*} was found [Pd(100); −0.419 eV → Pd(110); −0.244 eV → Pd(111); 0.154 eV → Pd(211); −0.134 eV]. Essentially, a larger compressive strain on the surface results in a lower magnitude of ΔG_{H*}, implying a more efficient HER performance. However, the Pd(211) surface yields a lower magnitude of ΔG_{H*} although it has a smaller compressive strain compared with the Pd(111) surface. Therefore, besides the strain, the surface orientation still influences the hydrogen adsorption ability.

Besides the effect of strain induced by an increasing number of PdH sublayers on the improved HER activity, we further investigated the sole strain effect (without PdH sublayers) on the H adsorption for all Pd surfaces. To this end, the ΔG_{H*} for Pd(111), Pd(110), Pd(100), and Pd(211) surfaces at low H* coverage, were calculated as a function of the compressive areal strain. In order to be consistent with the strain occurring by the formation of PdH sublayers, we applied the compressive areal strain of up to 4% to all pure Pd systems. As depicted in Figure S15 (Supporting Information), the magnitudes of the ΔG_{H*} for all pure surfaces decrease as the compressive areal strain increases indicating the enhanced HER activity, as similarly found in the case of the surfaces containing PdH sublayers. However, for this system, there is a smaller change in the ΔG_{H*} compared to the case with PdH sublayers (Figure 5). Comparing ΔG_{H*} of the pristine surfaces to the ones with the largest applied compressive areal strain (4%), the ΔG_{H*} changes from −0.427 to −0.375 eV, −0.367 to −0.350 eV, −0.474 to −0.469 eV, and −0.386 to −0.332 eV for Pd(111), Pd(110), Pd(100), and Pd(211), respectively. Remarkably, the Pd(100) surface is still relatively insensitive to the compressive strain.

From an electronic point of view, the decrease in the magnitude of adsorption energy of H* with increasing compressive strain can be understood by the increased overlap of the Pd d-orbitals, which results in increased bandwidth. To preserve the degree of electron filling, the position of the d-band of Pd shifts to a lower energy relative to the Fermi level. Upon H absorption, this downshifting of the position of the d-band results in the increased population of the H-s–Pd-d antibonding orbital, which weakens the adsorption of H* on the surface. That is, the position of the d-band of the surface that contains a higher number of PdH sublayers and a larger compressive strain, is far from the Fermi level (more negative value), indicating a weaker binding of H* on the surface (ΔG_{H*} gets closer to zero).

Already from the CV and XRD measurement (Section 2.1), the observation arose that the Pd surfaces are prone to change upon electrochemical cycling, which is likely connected to the absorption of hydrogen and subsequent strain effects, as discussed earlier. Therefore, we investigated the nature of active sites due to these changes by using n-EC-STM measurements after electrochemical cycling on Pd(111) and Pd(100). For both orientations, we observed a change in the morphology and, therefore, a change in the noise-behavior, as illustrated in **Figure 6**. Compared to the freshly annealed, atomically flat surface (Figure S4, Supporting Information), a "hilly" surface with

islands of ≈10–20 nm with a height of ≈0.3–1.5 nm appeared (Figure S16, Supporting Information). This is very likely caused by the release of strain, as it is also assured by the DFT data that the absorption of hydrogen leads to strain effects. As a possible result, the newly shaped surface is concave and convex curved. Another interesting observation is that apart from the morphology, also the nature of the active sites changed.

Figure 6a shows a 125 × 125 nm^2 area of cycled Pd(111), labeled as Pd(111)$_c$, with the potential set to −0.8 V_{Pt} for the upper half of the image (HER "On") and in the lower half to 0.0 V_{Pt} (HER "Off") in 0.1 M $HClO_4$. The color scheme highlights the difference between concavely (blue) and convexly curved (orange) areas. The exact separation of these different curved areas is illustrated in Figure S17a of the Supporting Information. Here, the noise, visible as white dots, was found predominantly in convex, but also in several concave curved areas for HER "On." While the concave curved areas have a similar activity all over, some concave curved areas show a relatively low and others a very high activity. A 3D view and a similar measurement can be seen in Figure S18b,d of the Supporting Information, showing the same trend. As visible in the histograms in Figure 6b, on average, concave curved areas show a similar behavior to convex curved areas. Compared to the flat relatively inactive terrace regions for the annealed crystal found in Figure 3a the electrocatalytic behavior at the cycled surface seems to be fundamentally different.

A significant change in the noise behavior was also observed for the cycled Pd(100), labeled Pd(100)$_c$, in Figure 6c. The concave curved areas show a very low activity compared to the convex curved areas. Similar 2D and 3D images of Pd(100) and the separation of the curved areas can be found in Figures S19 and S17b (Supporting Information), respectively. Here, for HER "On" the potential was set to −0.7 V_{Pt} and for HER "Off" to 0.0 V_{Pt}. This trend is verified in the plot in Figure 6d, which was calculated analogously to b), illustrating the difference between concave and convex curved areas. A much larger increase in the noise level was observed in the convex curved areas compared to the concave curved areas when the reaction was turned "On." In comparison to the noise behavior of the freshly annealed Pd(100) in Figure 3c, showing some activity all over the surface, here, the noise was predominantly found in convex curved regions. This is also visible in the line scan showing a 28 nm broad area which equals ≈100 Pd-atoms, with distinct noise spikes in the convex curved areas. An interesting conclusion is that steps seem to transform from being the most active on the freshly annealed surface (Figure 3a,c) to convex sites after electrochemical cycling (compare the step in Figure S19d (Supporting Information) in case of Pd(100)$_c$). The reason for this is most likely the changed hydrogen adsorption properties due to strain effects, as indicated by the DFT calculations. We can summarize that the absorption of hydrogen and the subsequent creation of strain changes the surface morphology and the nature of the active sites.

2.4. Design Principle of Pd Nanoparticles for Optimized HER Performance

From the previous discussions, it is clear that the strain induced by hydrogen absorption, as well as the average surface
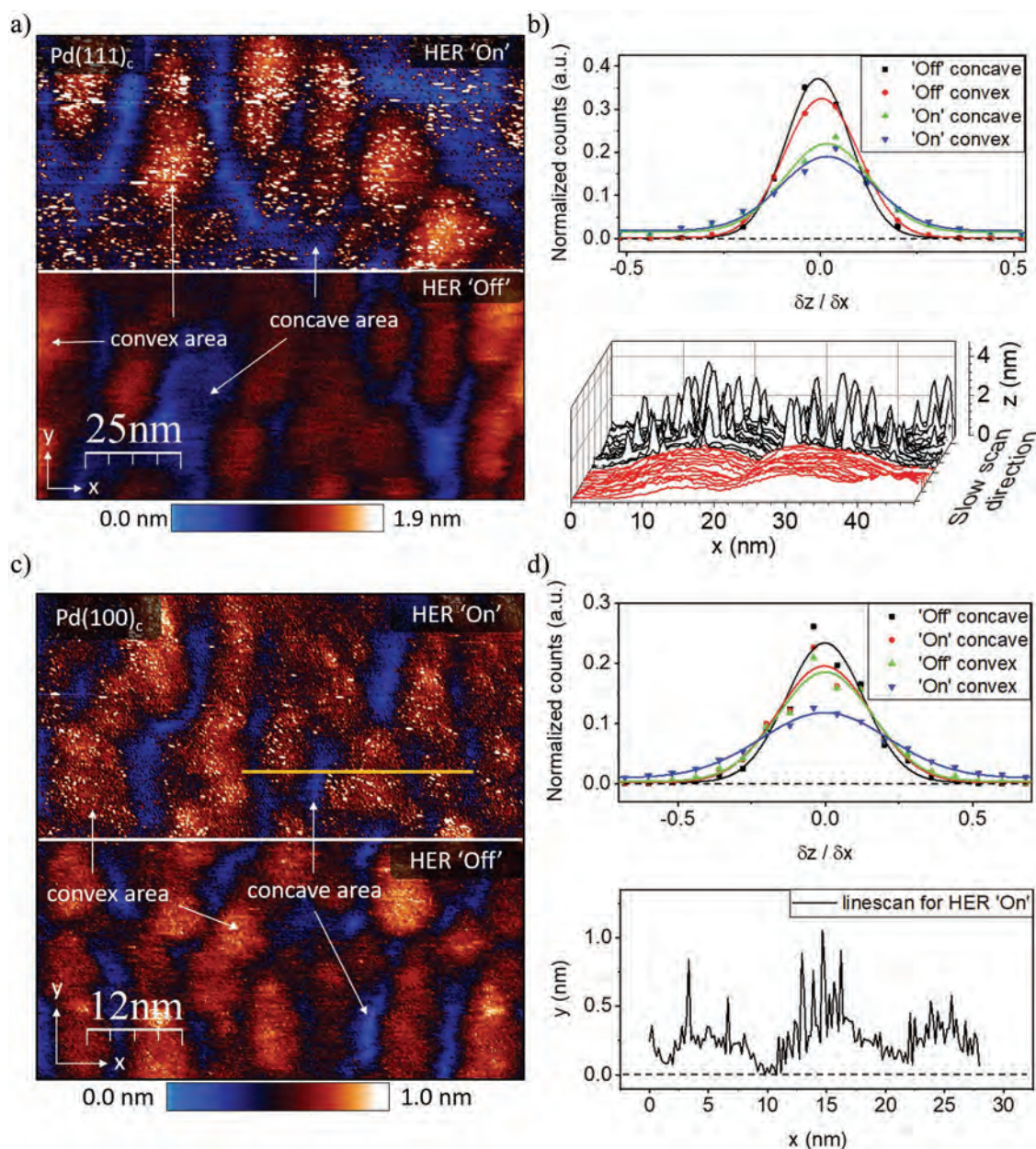
ADVANCED
SCIENCE NEWS
www.advancedsciencenews.com

NANO · MICRO
small
www.small-journal.com

Figure 6. n-EC-STM measurement of Pd(111)$_c$ and Pd(100)$_c$ after cyclic voltammetry in 0.1 M HClO$_4$ for HER turned "On" (-0.8 and -0.7 V$_{Pt}$, respectively) and "Off" (0.0 V$_{Pt}$). The blue-colored areas show the concave curved areas, while the convex ones are illustrated in orange color (separation of the areas is shown in Figure S17 of the Supporting Information). a) The convex areas of Pd(111) show high activity for reaction "On." Very active and mostly inactive sites were found in the concave curved areas. b) Normalized counts versus the derivative of the slopes of the concave and convex sites of a) showing the highest activities for convex areas followed closely by concave regions. The waterfall plot provides an additional perspective of a border between HER "On" (black) and HER "Off" (red) and the noise behavior at this interface (compare Figure S18a in the Supporting Information for the exact position). c) Analogous measurements for Pd(100) while in contrast to Pd(111) the concave curved areas are less active. d) The noise level of concave sites increases only slightly for reaction "On." In contrast, the convex area shows a high activity when the reaction is turned "On." The line scan shows the orange highlighted line in c) for HER "On," which has a length of 28 nm and therefore illustrates ≈100 Pd atoms. c) and d) are fitted by the Gaussian function.

coverage, plays a crucial role in the activity of Pd surfaces. Nevertheless, the Pd(111) and especially the Pd(211) surfaces can be classified as particularly active with respect to the HER. To boost its activity, for nanostructured catalysts, this means that these surfaces are to be maximized when normalized to the catalyst mass. This, in turn, implies for nanoparticles that due to their higher volume to surface ratios, only the smallest particles should be considered. On the other hand, one should not forget the critical role of the PdH subsurface layers. As shown in this study, one can optimize the binding energies by more than 200 meV due to induced strain. Therefore, a size of several nanometers is desirable, allowing to integrate sufficient
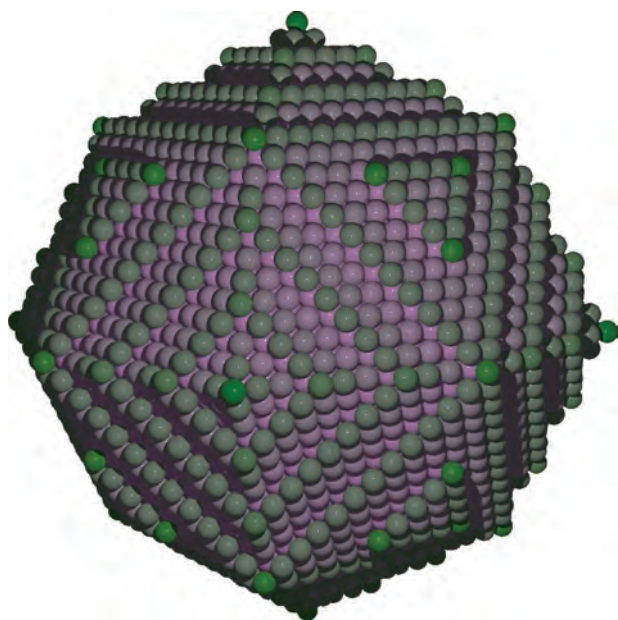
Figure 7. Schematic of a Pd nanoparticle with optimized surface morphology. The particle consisting of 8127 Pd atoms has an average diameter of 6.85 nm. It shows a high ratio of Pd(211) and Pd(111) surfaces which have shown to be highly active.

absorbed hydrogens in the subsurface layers. Considering these requirements and surface stability, we applied the Wulff construction to generate arbitrarily nanoparticles with predominantly Pd(211) and Pd(111) as exposed surfaces. One of the most promising candidates is displayed in **Figure 7**. This particle consisting of 8127 atoms has a diameter along the longest and shortest axis of 7.0 and 6.7 nm, respectively. It consists mainly of Pd(211) surfaces which are particularly active and Pd(111) surfaces. For better representation, the atoms are colored according to their coordination. Results for single crystal surfaces indicate that the active sites should be highly coordinated threefold (fcc hollow) at the step edges and on the Pd(111) planes.

3. Conclusion

The aim of this study was the characterization of the HER activity on model Pd surfaces, directing a particular focus on the effects of hydrogen absorption on the nature of the active sites. Pd(111) was identified to be the most stable basal plane by DFT calculations, followed by Pd(100) and Pd(110) surfaces. The experimental measurements showed the following HER activity trend: Pd(111) > Pd(110) > Pd(100). Using cyclic voltammetry and the XRD technique, we demonstrated that hydrogen absorption into the bulk changes the electrochemical behavior and increases the lattice parameter. EC-STM images provided further confirmation of the morphological transformation. The nature of HER active sites is likely affected by the generation of strain due to hydrogen absorption. This was supported by DFT calculations, which indicated that the population of Pd subsurface layers with H results in a compressive strain that lowers the magnitude of the H adsorption free energy on the low-index (111), (100), and (110) surfaces, thereby increasing the

HER activities on these surfaces. In the presence of strain, the DFT-calculated HER activities in the model surfaces were in the decreasing order of (211) > (111) > (110) > (100), in agreement with the experimental results. Further, using the impedance analysis, we estimated the surface coverage of Pd(111), Pd(110), and Pd(100) as ≈ 0, ≈ 0.3–0.4, and ≈ 0.95, respectively, and elucidated that the Heyrovsky mechanism is suppressed on all investigated Pd surfaces in acidic media. From the EC-STM measurements, we determined the most active sites on freshly annealed Pd(111) near step edges. More specifically, the upper edge seemed to be more active than the bottom of the step. In contrast, terraces remained less active. Interestingly, not all steps were equally active, which is explained by their different coordination. Similarly, freshly annealed Pd(100) showed the highest activity on step edges, although in this case, significant activity was found on the terrace as well. The absorption of hydrogen into the bulk during cyclic voltammetry results in a change of the surface morphology and distribution of the active sites at both crystalline planes. A hilly structure was observed, exhibiting significantly increased activity on convexly curved areas. For Pd(100)$_c$ the concave areas were less active than the convex areas. In contrast, for the Pd(111)$_c$, concave and convex curved areas possess a very similar activity. The alteration of crystal surface morphology is presumably induced by the absorption of hydrogen into the bulk during potential cycling. This induces strain which, in turn, changes the nature of active sites. Finally, a possible nanoparticle design was introduced, consisting of mostly Pd(211) and Pd(111) surfaces, as they show the best HER activity of all investigated planes in this study. In summary, this work combined theoretical and experimental approaches to elucidate the surface-activity relation for the HER on Pd model surfaces. The obtained results are indispensable for the general understanding of metal hydride systems and formulation of design principles for the optimal Pd-based nanostructured catalysts.

4. Experimental Section

In the following, the most relevant methods and techniques which were used for the calculations and measurements presented in this work will be discussed in detail. Tables including the most relevant settings used for the experiments are attached in Section S17 of the Supporting Information.

Sample and Electrolyte Preparation: For the experiments, Pd(111) (Ø 6 mm, 99.999%, MaTecK, Germany) and Pd(111), Pd(110), Pd(100) single crystals (Ø 5 mm, 99.999%, MaTecK, Jülich, Germany) disc electrodes were used. Each surface was prepared by the manufacturer with a roughness of less than 0.01 µm and an orientation accuracy better than 0.1°. Before each experiment, a well-orientated surface was assured by annealing in either a tubular furnace or an inductive heater setup. The Heraeus Instruments RO 7/50 furnace enables high-temperature annealing in an inert atmosphere to prevent oxidation of the Pd surface. The Pd crystal was placed in a small ceramic boat into the middle of a quartz tube fed by a continuous flow of Ar (Argon 5.0, Westfalen, Germany). After ≈1 h of heating, a temperature of 950 °C was reached and held for around three more hours. The cooling period to room temperature took ≈18 h. For further transportation and preparation, the single crystal's surface was covered with a drop of electrolyte inside the furnace to protect the freshly annealed surface from air. Alternatively, the usage of a high-frequency induction heater (20–80 kHz, 15 KW–EQ-SP-15A, MTI, USA) with a maximum output power of 15 kW was

ADVANCED
SCIENCE NEWS
www.advancedsciencenews.com

NANO · MICRO
small
www.small-journal.com

introduced. The Pd crystals were placed into a special compartment which enabled a pure Ar atmosphere. The crystal was annealed three times with a first heating period of 90 s and each following 60 s and a relaxation time of 5 min in between. Again, to avoid exposure to air, the surface was protected with a drop of the electrolyte after the annealing process. The 0.1 M $HClO_4$ electrolytes were prepared by diluting 70% perchloric acid (Suprapur, Merck, Germany) using ultrapure water (Evoqua Milli-Q (18.2 $M\Omega$ cm)).

Cyclic Voltammetry and Activity Measurements: Before the electrochemical measurements, all glassware and experimental cells were cleaned with a 3:1 mixture of sulfuric acid (96% H_2SO_4 Suprapur, Merck, Germany) and hydrogen peroxide (30% H_2O_2, Suprapur, Merck, Germany), and subsequently washed by boiled ultrapure water for several times. All experiments were controlled by a VSP-300 potentiostat (Bio-Logic, France). The working electrode (WE) was immersed into the electrolyte at a starting potential of 0.57 V_{RHE} in order to minimize possible electrochemical surface processes beforehand. A mercury–mercury sulfate (MMS) and a curled polycrystalline Pd-wire ($\varnothing$ = 0.25 mm, 99.95%, MaTecK, Jülich, Germany) were used as a reference and counter electrode (CE), respectively. The quality of the annealed single crystalline surface was confirmed by CVs in Ar-saturated 0.1 M $HClO_4$ in the potential range between 0.2 and 1.2 V_{RHE} at a scan rate of 50 mV s^{-1}. Polarization curves for evaluating the HER activity were recorded in a hanging meniscus configuration in H_2-saturated electrolyte. The potential range was set between −0.18 and 0.52 V_{RHE} at a scan rate of 50 mV s^{-1}. However, the HER activity evaluation was performed in the potential interval from −0.18 to 0.22 V_{RHE}. In this configuration, the risk of mass transfer limitations is limited since the HER over Pd in comparison to other catalysts is considerably slower. Further, hydrogen is essentially absorbed into the bulk. Thus, no gas bubbles are present at the electrode, which allows taking benefit of the full mass transfer rate from the electrolyte to the surface. More information about the experimental settings for each measurement is shown in Table S5 in the Supporting Information.

Electrochemical Impedance Measurements: Impedance spectra were acquired in 10 mV steps between 0.00 and −0.05 V_{RHE}. For this, a perturbation amplitude of 10 mV was applied, and spectra were recorded in a frequency range between 30 kHz and 0.1 Hz. The 0.1 M $HClO_4$ electrolyte was saturated with argon before and during the measurements. To compensate for measurement artifacts caused by the impedance of the RE in the high-frequency regime, a shunt capacitor was connected between the RE and an additional Pt wire. This wire was immersed in the electrolyte in the proximity of the tip of the Luggin-capillary. The quality of the recorded spectra was verified by a Krammer–Kroenig check. The impedance data were analyzed using the homemade software EIS Data Analysis 1.3.[70,71]

Grazing-Incidence X-Ray Diffraction Measurements: Grazing-incidence X-ray Diffraction (GIXRD) patterns of the Pd(111) single crystal in the pristine state and after six cycles of HER (potential range between −0.18 and 0.22 V_{RHE}) were collected on an X'Pert PRO PANanalytical instrument with a Ni-filtered Cu Kα radiation (λ = 1.5406 Å). The procedure used for GIXRD measurements consisted of a 2Theta range of 35°–90° and a slow-scanning step of 2° min^{-1}. The settings used for each GIXRD measurement can be found in Table S6 in the Supporting Information.

EC-STM Measurements: The EC-STM measurements were performed by a Nanoscope III SPM Multimode from Veeco Instruments with a Veeco Nanoscope Universal bipotentiostat connected to a Nanoscope IIID controller. The STM-tips were mechanically ripped from a platinum/iridium (Pt80/Ir20, $\varnothing$ = 0.25, 99.9+%, Goodfellow GmbH) wire with a side cutter. To minimize the impact of reactions at the tip-electrolyte interface on the tunneling signal, the tip was insulated by Apiezon wax.[72] The sample was clamped between a Teflon ring and a steel plate fixed with screws acting as a miniature electrochemical cell. For all measurements a Pt wire ($\varnothing$ 0.5 mm, 99.99%, MaTecK, Germany) as a quasi–RE and a curled Pd wire ($\varnothing$ 0.25 mm, 99.95%, MaTecK, Germany) as a CE were used. Detailed information about the values set for each STM measurement can be found in Table S7 in the Supporting Information.

Noise-EC-STM Technique: The innovative idea of the noise-electrochemical scanning tunneling microscopy (n-EC-STM) technique is to identify active sites by analyzing the noise in the STM signal under reaction conditions as first published by Pfisterer et al.[42] An ongoing electrochemical reaction will persistently change the electrolyte composition and structure in the tunneling barrier between the scanning tip and the WE. The movement of ions in the tunneling barrier, as well as the structure of the electrolyte has been shown to influence the tunneling barrier and thus the STM signal.[73–80] Therefore, if the tip is placed over an active area, the detected tunneling current varies with time and a noisy signal is detected. Most likely, this is a direct consequence of the ad- or absorption of molecules on the surface. In contrast, in areas with low electrochemical activity, the detected noise level is significantly lower. Thus, the noise level of the STM signal serves as a tool to detect the active sites. All STM measurements were performed in air atmosphere at room temperature and evaluated using WSxM 5.0 Develop 9.4.[81]

Noise Analysis: For this evaluation, the STM signal (here, height *z*) is derived in the fast scan direction *x* according to the "numpy.gradient()" function of the python's library NumPy. Here the different derivatives of the slopes between neighboring data points of each line scan were plotted versus its normalized quantity and were fitted afterward. Detailed information of the working principle can be found at the NumPy website[82] and in refs. [83,84, and 85]. Subsequently, histograms are compiled from the signal derivatives. In this work, bin sizes of 0.08 were used, except for Figure 3d, which was rendered using a bin size of 0.03 for Pd(100). At high noise levels, the derivative values (slopes in line scans) possess a broad FWHM and low-intensity distribution. Therefore, the width and height of an adequate fit of the histograms serve as a quantification of the noise level.[57]

DFT Calculations: First-principles calculations based on spin-polarized DFT approach were performed using the Vienna Ab Initio Simulation Package (VASP 5.4).[86,87] The projector augmented-wave (PAW) method[88,89] was employed to describe the electron-ionic core interactions where Pd 4d^{10} and H 1s^1 were treated as valence electrons. Their wavefunctions were expanded with the plane-wave basis using a cutoff energy of 500 eV. The exchange-correlation functional was approximated using the generalized gradient approximation (GGA) in the form of Perdew, Burke, and Ernzerhof (PBE).[90] To account for the van der Waals interactions, the lattice constants of a bulk face-centered cubic (fcc) Pd were calculated using various dispersion correction methods, as summarized in Table S8 (Supporting Information). It can be found that the obtained lattice constant (3.891 Å) using the DFT-D3(BJ) approach proposed by Grimme et al.[91] is closest to the experimental value (3.890 Å), which was determined using XRD in this work (Figure 1e) and other experimental studies.[92,93] Therefore, the DFT-D3(BJ) approach was used for all subsequent calculations. All structures were optimized using the conjugate gradient method.[94] The Methfessel–Paxton smearing technique[95] (σ = 0.05 eV) was used during the geometry optimization.

Different Pd surfaces were modeled by cleaving the optimized structure of a bulk fcc Pd unit cell (containing 4 atoms) in the low-index Pd(111), Pd(110), and Pd(100) facets for the flat surfaces, as well as the Pd(211) facet for the stepped surface. The Pd(111) and Pd(211) surfaces were obtained using a 1 × 1 unit cell, while Pd(100) and Pd(110) surfaces were constructed using a 2 × 1 supercell, containing four Pd atoms per layer for Pd(111), Pd(110), and Pd(100) surfaces and six Pd atoms per layer for Pd(211) surface. In order to investigate the H adsorption on Pd surfaces with different numbers of PdH sublayers (up to 4 sublayers), the appropriate slab thickness was determined. Here, the thickness of the Pd(111) surface was used as a criterion for the other three surfaces. Therefore, these slabs were built with the thickness of seven (13.48 Å), eleven (13.76 Å), eight (13.62 Å), and seven (14.30 Å) atomic layers for (111), (110), (100), and (211) surfaces, respectively. A vacuum space of 20 Å along the *z* direction was added to avoid interaction between the periodic images. Figure S20 (Supporting Information) illustrates the top and side views of these surfaces. During the structural relaxation of the slabs, the two bottom layers (2.25, 1.95, and 2.38 Å) for Pd(111), Pd(100), and Pd(211) surfaces, respectively, and the three bottom layers

(2.75 Å) for Pd(110) surface, were completely fixed to mimic its bulk structure. The sampling of the Brillouin zone using the Monkhorst-Pack scheme[96] was employed with $7 \times 7 \times 7$ and $7 \times 7 \times 1$ k-points for bulk and slabs calculations, respectively. The structures were fully optimized until the force acting on each atom was less than 0.01 eV Å^{-1}. The energy of convergence tolerance was set to 1×10^{-6} eV. The electric dipole correction in the z direction was used to cut the furious interaction between the repeated images of the slab model. The H$_2$ molecule was modeled using one free molecule inside a $20 \times 20 \times 20$ Å^3 supercell with electric dipole correction implemented in all directions. To study the H diffusion mechanism, the CI-NEB approach was carried out to determine the minimum energy path of H diffusion. The CI-NEB method allows for ionic relaxation of each configuration along the diffusion path. The transition state (TS) is located at the saddle point of the reaction coordinate, where the energy difference between TS and the initial state yields the diffusion barrier.

Supporting Information

Supporting Information is available from the Wiley Online Library or from the author.

Acknowledgements

Conflict of Interest

The authors declare no conflict of interest.

Data Availability Statement

The data that support the findings of this study are available from the corresponding author upon reasonable request.

Keywords

[1] U. Nations, *The Paris Agreement*, **1998**, https://unfccc.int/process/conferences/pastconferences/paris-climate-change-conference-november-2015/paris-agreement (accessed: March 2022).
[2] *The Sustainable Development Goals 2016. eSocialSciences*, UN, New York **2016**.
[3] A. Züttel, A. Remhof, A. Borgschulte, O. Friedrichs, *Philos. Trans. R. Soc., A* **2010**, *368*, 3329.
[4] N. L. Garland, D. C. Papageorgopoulos, J. M. Stanford, *Energy Procedia* **2012**, *28*, 2.
[5] J. Rogelj, O. Geden, A. Cowie, A. Reisinger, *Nature* **2021**, *591*, 365.
[6] H. Kasai, A. A. B. Padama, B. Chantaramolee, R. L. Arevalo, *Hydrogen and Hydrogen-Containing Molecules on Metal Surfaces*, Springer, Singapore **2020**.
[7] Y. Dou, L. Sun, J. Ren, L. Dong, *Hydrogen Economy*, Elsevier, New York **2017**, p. 277.
[8] B. C. Tashie-Lewis, S. G. Nnabuife, *Chem. Eng. J. Adv.* **2021**, *8*, 100172.
[9] Y. E. Cheon, M. P. Suh, *Angew. Chem., Int. Ed.* **2009**, *48*, 2899.
[10] A. Zalineeva, S. Baranton, C. Coutanceau, G. Jerkiewicz, *Sci. Adv.* **2017**, *3*, e1600542.
[11] S. Mubeen, T. Zhang, B. Yoo, M. A. Deshusses, N. V. Myung, *J. Phys. Chem. C* **2007**, *111*, 6321.
[12] X. Zeng, M. Latimer, Z. Xiao, S. Panuganti, U. Welp, W. Kwok, T. Xu, *Nano Lett.* **2011**, *11*, 262.
[13] M. Wilde, K. Fukutani, W. Ludwig, B. Brandt, J. H. Fischer, S. Schauermann, H. J. Freund, *Angew. Chem., Int. Ed.* **2008**, *47*, 9289.
[14] S. Katano, H. S. Kato, M. Kawai, K. Domen, *J. Phys. Chem. B* **2003**, *107*, 3671.
[15] W. Wang, X. Pan, X. Zhang, W. Yang, G. Xiong, *Sep. Purif. Technol.* **2007**, *54*, 262.
[16] S. Adhikari, S. Fernando, *Ind. Eng. Chem. Res.* **2006**, *45*, 875.
[17] Z. Zhao, X. Huang, M. Li, G. Wang, C. Lee, E. Zhu, X. Duan, Y. Huang, *J. Am. Chem. Soc.* **2015**, *137*, 15672.
[18] J. Zhang, M. Chen, H. Li, Y. Li, J. Ye, Z. Cao, M. Fang, Q. Kuang, J. Zheng, Z. Xie, *Nano Energy* **2018**, *44*, 127.
[19] A. Lasia, *Int. J. Hydrogen Energy* **2019**, *44*, 19484.
[20] G. Yang, S. A. Akhade, X. Chen, Y. Liu, M. S. Lee, V. A. Glezakou, R. Rousseau, J. A. Lercher, *Angew. Chem., Int. Ed.* **2019**, *58*, 3527.
[21] T. C. Narayan, F. Hayee, A. Baldi, A. Leen Koh, R. Sinclair, J. A. Dionne, *Nat. Commun.* **2017**, *8*, 14020.
[22] X. Zhao, L. Ma, *Int. J. Hydrogen Energy* **2009**, *34*, 4788.
[23] L. A. Kibler, *ChemPhysChem* **2006**, *7*, 985.
[24] J. D. Benck, A. Jackson, D. Young, D. Rettenwander, Y.-M. Chiang, *Chem. Mater.* **2019**, *31*, 4234.
[25] B. D. Adams, A. Chen, *Mater. Today* **2011**, *14*, 282.
[26] A. Knapton, *Platinum Met. Rev.* **1977**, *21*, 44.
[27] M. Skottke, R. J. Behm, G. Ertl, V. Penka, W. Moritz, *J. Chem. Phys.* **1987**, *87*, 6191.
[28] R. Behm, K. Christmann, G. Ertl, *Surf. Sci.* **1980**, *99*, 320.
[29] T. Felter, E. C. Sowa, M. Van Hove, *Phys. Rev. B* **1989**, *40*, 891.
[30] C. Nyberg, C. Tengstål, *Solid State Commun.* **1982**, *44*, 251.
[31] F. Netzer, M. El Gomati, *Surf. Sci.* **1983**, *124*, 26.
[32] H. Conrad, G. Ertl, E. Latta, *Surf. Sci.* **1974**, *41*, 435.
[33] T. Harumoto, Y. Ohnishi, K. Nishio, T. Ishiguro, J. Shi, Y. Nakamura, *AIP Adv.* **2017**, *7*, 065108.
[34] D. Teschner, A. Pestryakov, E. Kleimenov, M. Hävecker, H. Bluhm, H. Sauer, A. Knop-Gericke, R. Schlögl, *J. Catal.* **2005**, *230*, 186.
[35] M. S. Daw, S. M. Foiles, *Phys. Rev. B* **1987**, *35*, 2128.
[36] O. B. Christensen, P. Stoltze, K. W. Jacobsen, J. Nrskov, *Phys. Rev. B* **1990**, *41*, 12413.
[37] N. Ozawa, T. A. Roman, H. Nakanishi, H. Kasai, N. B. Arboleda Jr., W. A. Diño, *J. Appl. Phys.* **2007**, *101*, 123530.
[38] S. Ohno, M. Wilde, K. Fukutani, *J. Chem. Phys.* **2014**, *140*, 134705.

ADVANCED
SCIENCE NEWS
www.advancedsciencenews.com

NANO · MICRO
small
www.small-journal.com

[39] M. Fleischmann, S. Pons, M. Hawkins, *Electrochemically Induced Nuclear Fusion of Deuterium*, Elsevier, Sequoia **1989**.

[40] E. Gibney, *Nature* **2019**, *569*, 611.

[41] P. Ball, *Nature* **2019**, *569*, 601.

[42] J. H. Pfisterer, Y. Liang, O. Schneider, A. S. Bandarenka, *Nature* **2017**, *549*, 74.

[43] T. Kosmala, A. Baby, M. Lunardon, D. Perilli, H. Liu, C. Durante, C. Di Valentin, S. Agnoli, G. Granozzi, *Nat. Catal.* **2021**, *4*, 850.

[44] Y.-N. Wen, J.-M. Zhang, *Solid State Commun.* **2007**, *144*, 163.

[45] B. Fu, W. Liu, Z. Li, *Appl. Surf. Sci.* **2010**, *256*, 6899.

[46] L. L. Jewell, B. H. Davis, *Appl. Catal., A* **2006**, *310*, 1.

[47] K. Naito, M. Nakamura, O. Sakata, N. Hoshi, *Electrochemistry* **2011**, *79*, 256.

[48] N. Hoshi, M. Noma, T. Suzuki, Y. Hori, *J. Electroanal. Chem.* **1997**, *421*, 15.

[49] F. J. Sarabia, V. Climent, J. M. Feliu, *ChemPhysChem* **2019**, *20*, 3056.

[50] M.-S. Zei, T. Lei, G. Ertl, *Z. Phys. Chem.* **2003**, *217*, 447.

[51] T. Shinagawa, A. T. Garcia-Esparza, K. Takanabe, *Sci. Rep.* **2015**, *5*, 13801.

[52] Z. Zhao, M. M. Flores Espinosa, J. Zhou, W. Xue, X. Duan, J. Miao, Y. Huang, *Nano Res.* **2019**, *12*, 1467.

[53] S. Watzele, J. Fichtner, B. Garlyyev, J. N. Schwämmlein, A. S. Bandarenka, *ACS Catal.* **2018**, *8*, 9456.

[54] A. Lasia, *Modern Aspects of Electrochemistry*, Springer, Boston, MA **2002**.

[55] R. W. Haid, R. M. Kluge, T. O. Schmidt, A. S. Bandarenka, *Electrochim. Acta* **2021**, *382*, 138285.

[56] R. M. Kluge, R. W. Haid, I. E. L. Stephens, F. Calle-Vallejo, A. S. Bandarenka, *Phys. Chem. Chem. Phys.* **2021**, *23*, 10051.

[57] R. W. Haid, R. M. Kluge, Y. Liang, A. S. Bandarenka, *Small Methods* **2021**, *5*, 2000710.

[58] Y. Liang, C. Csoklich, D. McLaughlin, O. Schneider, A. S. Bandarenka, *ACS Appl. Mater. Interfaces* **2019**, *11*, 12476.

[59] M. Lunardon, T. Kosmala, C. Durante, S. Agnoli, G. Granozzi, *Joule* **2022**, *6*, 617.

[60] L. Cser, G. Török, G. Krexner, M. Prem, I. Sharkov, *Appl. Phys. Lett.* **2004**, *85*, 1149.

[61] E. Klotz, B. Mattson, *J. Chem. Educ.* **2009**, *86*, 465.

[62] D. Long, M. Li, D. Meng, Y. He, I. T. Yoon, R. Ahuja, W. Luo, *Int. J. Hydrogen Energy* **2018**, *43*, 18372.

[63] L. Isaeva, D. Bazhanov, E. Isaev, S. Eremeev, S. Kulkova, I. Abrikosov, *Int. J. Hydrogen Energy* **2011**, *36*, 1254.

[64] W. Dong, V. Ledentu, P. Sautet, A. Eichler, J. Hafner, *Surf. Sci.* **1998**, *411*, 123.

[65] M. Johansson, E. Skulason, G. Nielsen, S. Murphy, R. M. Nielsen, I. Chorkendorff, *Surf. Sci.* **2010**, *604*, 718.

[66] N. Ozawa, T. A. Roman, H. Nakanishi, H. Kasai, N. B. Arboleda Jr., W. A. Diño, *J. Appl. Phys.* **2007**, *101*, 123530.

[67] J. Völkl, G. Alefeld, *Hydrogen in Metals I*, Springer, Berlin **1978**.

[68] J. K. Nørskov, T. Bligaard, A. Logadottir, J. Kitchin, J. G. Chen, S. Pandelov, U. Stimming, *J. Electrochem. Soc.* **2005**, *152*, J23.

[69] H. A. Aleksandrov, S. M. Kozlov, S. Schauermann, G. N. Vayssilov, K. M. Neyman, *Angew. Chem.* **2014**, *126*, 13589.

[70] A. S. Bondarenko, *Anal. Chim. Acta* **2012**, *743*, 41.

[71] A. S. Bandarenka, *Lect. Notes Impedance Spectrosc.* **2013**, *4*, 29.

[72] L. Nagahara, T. Thundat, S. Lindsay, *Rev. Sci. Instrum.* **1989**, *60*, 3128.

[73] G. Binnig, H. Fuchs, E. Stoll, *Surf. Sci. Lett.* **1986**, *169*, L295.

[74] M. Sumetskii, A. Kornyshev, U. Stimming, *Surf. Sci.* **1994**, *307*, 23.

[75] J. Dunphy, P. Sautet, D. Ogletree, O. Dabbousi, M. Salmeron, *Phys. Rev. B* **1993**, *47*, 2320.

[76] T. Tiedje, J. Varon, H. Deckman, J. Stokes, *J. Vac. Sci. Technol., A* **1988**, *6*, 372.

[77] J. Pan, T. Jing, S. Lindsay, *J. Phys. Chem.* **1994**, *98*, 4205.

[78] A. Vaught, T. Jing, S. Lindsay, *Chem. Phys. Lett.* **1995**, *236*, 306.

[79] G. Nagy, T. Wandlowski, *Langmuir* **2003**, *19*, 10271.

[80] R. Hiesgen, D. Eberhardt, D. Meissner, *Surf. Sci.* **2005**, *597*, 80.

[81] I. Horcas, R. Fernández, J. Gomez-Rodriguez, J. Colchero, J. Gómez-Herrero, A. Baro, *Rev. Sci. Instrum.* **2007**, *78*, 013705.

[82] NumPy Developers, Routines webpage for numpy.gradient, https://numpy.org/doc/stable/reference/generated/numpy.gradient.html#numpy-gradient (accessed: March 2022).

[83] A. Quarteroni, R. Sacco, F. Saleri, *Numerical Mathematics*, Springer, Berlin, Heidelberg **2007**.

[84] D. R. Durran, *Numerical Methods for Wave Equations in Geophysical Fluid Dynamics*, Springer Science & Business Media, New York **2013**.

[85] B. Fornberg, *Math. Comput.* **1988**, *51*, 699.

[86] G. Kresse, J. Furthmüller, *Phys. Rev. B* **1996**, *54*, 11169.

[87] G. Kresse, J. Furthmüller, *Comput. Mater. Sci.* **1996**, *6*, 15.

[88] P. E. Blöchl, *Phys. Rev. B* **1994**, *50*, 17953.

[89] G. Kresse, D. Joubert, *Phys. Rev. B* **1999**, *59*, 1758.

[90] J. P. Perdew, K. Burke, M. Ernzerhof, *Phys. Rev. Lett.* **1996**, *77*, 3865.

[91] S. Grimme, J. Antony, S. Ehrlich, H. Krieg, *J. Chem. Phys.* **2010**, *132*, 154104.

[92] T. B. Flanagan, W. Oates, *Annu. Rev. Mater. Sci.* **1991**, *21*, 269.

[93] B. D. Adams, G. Wu, S. Nigro, A. Chen, *J. Am. Chem. Soc.* **2009**, *131*, 6930.

[94] I. Štich, R. Car, M. Parrinello, S. Baroni, *Phys. Rev. B* **1989**, *39*, 4997.

[95] M. Methfessel, A. Paxton, *Phys. Rev. B* **1989**, *40*, 3616.

[96] H. J. Monkhorst, J. D. Pack, *Phys. Rev. B* **1976**, *13*, 5188.